Surface & Coatings Technology 521 (2026) 133137

Contents lists available at ScienceDirect

Surface & Coatings Technology

journal homepage: www.elsevier.com/locate/surfcoat

Improving the manufacturability and assessing the performance of rare earth zirconates for thermal barrier coatings☆

Luis Isern [a,*], Koldo Almandoz Forcen [a], Christine Chalk [a], Gyaneshwara Brewster [b], Alan Johnstone [b], John Nicholls [a]

[a] Centre for Materials, Faculty of Engineering and Applied Sciences, Cranfield University, Cranfield, MK43 0AL, UK
[b] Rolls-Royce Plc, Derby, DE24 8BJ, UK

ARTICLE INFO

Keywords:
Rare-earth zirconates
Thermal barrier coatings
TBC
Electron-beam physical vapour deposition
EB-PVD
Calcium-magnesium-alumino-silicates
CMAS
Erosion
Morphology
Coatings

ABSTRACT

Key aero-engine components are subject to gas stream temperatures above the melting point of their metal alloy, a demanding environment that requires the deployment of thermal barrier coatings (TBCs) for their operation. Electron-beam physical vapour deposition (EB-PVD) can produce TBCs with unique columnar microstructures, conferring them the strain compliance required to survive in the cyclic, high-strain, high-thermal load environment experienced by the rotating parts of the high-temperature turbine. Rare earth zirconates (REZs) are proposed as substitute materials of partially-yttria-stabilised zirconia (PYSZ) to operate at higher temperatures due to their ability to withstand CMAS (calcium-magnesium-alumino-silicate) attack. On the other hand, the lower toughness of REZs makes them more susceptible to erosion damage during service, and some manufacturability issues have been noticed in previous studies. The current paper evaluates the manufacturability, CMAS resistance and erosion resistance of PYSZ and three REZ systems: gadolinium (GZ), neodymium (NZ) and lanthanum (LZ) zirconate. For the first time, successful NZ TBCs have been produced by EB-PVD, presenting a similar morphology, ease of manufacture and CMAS resistance to GZ, but inferior erosion resistance. LZ has compositional banding, lacks columnarity in La-rich regions, and has the lowest CMAS and erosion resistance of the REZs investigated. Co-evaporation of lanthana and PYSZ ingots increased compositional homogeneity of LZ, but the increased La content of the unoptimised process makes the coatings hygroscopic. The erosion resistance of the REZs is 6–10 times lower than PYSZ, but the study of their failure mechanisms indicates a potential improvement strategy by altering the coating morphology.

1. Introduction

Thermal barrier coatings (TBCs) are sophisticated coating systems that protect the components located in the hottest parts of the turbine engine, allowing manufacturers to increase their engine operating temperatures and thus increase efficiency, which reduces fuel consumption and CO_2 emissions. The TBCs consist of a bondcoat that provides oxidation protection and improves adhesion of the outer layers, a thermally grown oxide (TGO) layer, usually alpha-alumina, that grows due to oxidation of the bondcoat, and a ceramic topcoat that, in conjunction with adequate cooling, provides a thermal gradient that reduces the temperature experienced by the single crystal nickel-superalloy substrates. The ceramic topcoat, often referred to as the TBC on its own, can be deposited by plasma-spray methods for increased thermal insulation and decreased cost (usually on stationary parts), or by electron-beam physical vapour deposition (EB-PVD) for increased strain compliance of the topcoat (usually on rotating parts and some vanes). The material of choice for the topcoat was traditionally zirconia partially stabilised with yttria (PYSZ) but, since the turn of the century, the rare earth zirconate (REZ) family has been proposed as alternative materials for increased operating temperatures [1–3].

One of the key aspects that make REZs attractive as TBC materials is their interaction with the particles that are ingested into the engine during operation. Those particles are predominantly a Calcium-Magnesium-Aluminosilicate (CMAS) with a variable composition across geographical locations. A representative composition ($C_{33}M_9A_{13}S_{45}$), widely used in the laboratory, initiates melt at 1230 °C, with other compositions having eutectic points lower than 1200 °C

☆ This article is part of a Special issue entitled: 'SVC 2025 TechCon' published in Surface & Coatings Technology.

* Corresponding author.
E-mail address: l.isernarrom@cranfield.ac.uk (L. Isern).

https://doi.org/10.1016/j.surfcoat.2025.133137
Received 11 September 2025; Received in revised form 18 December 2025; Accepted 28 December 2025
Available online 29 December 2025
0257-8972/© 2025 The Authors. Published by Elsevier B.V. This is an open access article under the CC BY license (http://creativecommons.org/licenses/by/4.0/).

[4,5], providing a simulation of behaviour at relevant temperatures for engine operation. EB-PVD PYSZ is susceptible to infiltration by molten CMAS down the vertical pores of its columnar structure, as illustrated in Fig. 1, losing strain compliance, and degrading due to the CMAS slag. By contrast, REZ TBCs rapidly react with CMAS, precipitating crystalline products that block the vertical porosity and effectively stop infiltration [6]. Other advantages of REZ over PYSZ are their increased phase stability, lower thermal conductivity, and increased sintering resistance [2,3]. Because of these advantages, many subsequent studies worked on the deposition of REZ TBCs by EB-PVD, especially for gadolinium zirconate $Gd_2Zr_2O_7$ (GZ) [1,7], samarium zirconate $Sm_2Zr_2O_7$ [8] and lanthanum zirconate $La_2Zr_2O_7$ (LZ) [9,10]. However, some initial studies e.g. [11] noticed difficulties in the deposition of those systems in the form of compositional fluctuations, which notably affected the LZ system which also tends to lack a defined columnar structure [9,10,12]. In addition, the pyrochlore structure of the REZ lacks the ferroelastic toughening mechanism exhibited by PYSZ, and thus is more susceptible to damage by erosion of solid particles by up to an order of magnitude [13], which happens when particles impact the top of the TBC.

This paper investigates the root causes of the challenges in the deposition process of three REZ systems by EB-PVD and provides a qualitative assessment of their performance against CMAS attack and erosion by solid particles, including PYSZ benchmark results. A novel TBC system is proposed, neodymium zirconate (NZ), of which early studies in pellet form showed promising results due to its high maximum use temperature and low thermal conductivity [3], but that, to the author's knowledge, has not been reported deposited by EB-PVD. The more mature GZ is evaluated as a benchmark system, and the study also includes the analysis of LZ, of special interest due to low thermal conductivity and high thermal stability despite difficulties in deposition [10]. Special focus has been placed on the manufacturability of LZ coatings based on three criteria: ease of evaporability, ability to form a columnar structure, and homogeneity of composition. Optimising the evaporation conditions is challenging as the available window of the main processing variables (pressure, temperature, sample rotation…) is limited. Co-evaporation of PYSZ and La_2O_3 ingots has been performed to circumvent those limitations, to confirm the role of partial pressure in composition banding, and to evaluate its effectiveness as a potential solution to the root causes of manufacturability issues of LZ. The performance of the REZ and PYSZ systems in stopping CMAS infiltration has been evaluated by measuring thickness loss and assessing the depth of penetration of Ca, Mg, Al and Si via elemental analysis, and the blocking mechanisms of the different systems have been compared. The resistance to erosion by high-velocity impact of solid particles has been quantified for the four materials by mass loss and volume loss. Special focus has been given to identifying the erosion mechanisms of the REZ, studying the role of coating morphology, and assessing the effect of compositional heterogeneity.

2. Experimental methods

2.1. Coating deposition

All samples for this work were produced at Cranfield University by coating a commercial substrate with a TBC system. Samples destined for general inspection and erosion testing comprised a 25 × 25 mm and 1.6 mm-thick Ni—Cr alloy substrate (Nimonic 75, William Gregor Ltd., UK) with one face ground to 1200 grit, which was lightly grit-blasted (220 grit, 20 psi) and cleaned before aluminising by a gas-phase Chemical Vapour Deposition (CVD) process to produce a bondcoat and subsequently coated with a ceramic topcoat by Electron-Beam Physical Vapour Deposition (EB-PVD). Samples destined for CMAS testing will experience a temperature close to or higher than the melting point of Nimonic 75; therefore, 12.7 mm-diameter times 0.6 mm-thick

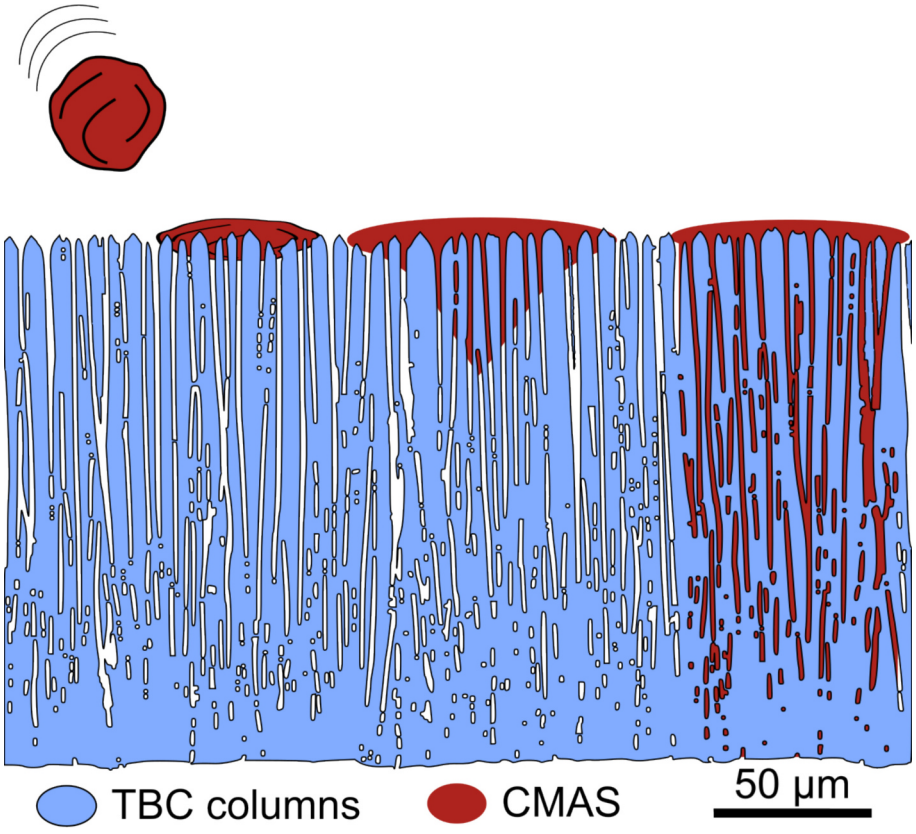


Fig. 1. Diagram of CMAS infiltration on a TBC deposited by EB-PVD. From left to right, the CMAS particles approach the coating, impact, melt, and infiltrate down the columnar interspace.

polycrystalline alumina discs (Pi-KEM, UK) of roughness $R_a = 0.67$ μm were used as substrates, which were directly coated with a ceramic topcoat by EB-PVD without a bondcoat.

The bondcoats were produced by gas-phase aluminising via CVD in the CVD rig at Cranfield University. This is a high-temperature, low-activity process using Al—Cr chips as source material and AlF_3 as activator at 1030 °C under Ar at ambient pressure. The Al diffusion results in a graded composition that is predominantly stoichiometric β-phase NiAl of around 20–30 μm with a roughness of $R_a = 0.48$ μm.

The topcoats were deposited using Cranfield University's customised system based on a EBS150/40 EB-PVD coater from Von Ardenne GmbH (Germany) with an EH150V electron-beam gun (150 kW maximum power, 40 kV acceleration voltage). The ceramics were deposited from 39.5 mm-diameter ceramic ingots of the following compositions: PYSZ as reference (7 wt% Y_2O_3, 93 wt% ZrO_2) [manufactured by Phoenix Coating Resources, subsidiary of Saint-Gobain, US], Gadolinium Zirconate $Gd_2Zr_2O_7$ (GZ) [manufactured by Phoenix Coating Resources, subsidiary of Saint-Gobain, US], Neodymium Zirconate $Nd_2Zr_2O_7$ (NZ) [manufactured by TCI Ceramics Inc., US], and Lanthanum Zirconate (LZ) 97 wt% $La_2Zr_2O_7$ and 3 wt% Y_2O_3 [manufactured by TCI Ceramics Inc., US] – note that the addition of yttria follows the recommendations of previous studies by Schultz's group [9]. A 7YSZ interlayer of 20–30 μm was first deposited, prior to the three Rare-Earth Zirconates (REZ), to avoid the degradation of the Thermally Grown Oxide (TGO) by forming RE-Al mixed oxides. The interlayer was deposited in the same run as the topcoat REZ, immediately before, under the same conditions and without breaking vacuum; the Cranfield EB-PVD coater can host up to three different ingots and the Von Ardenne gun can evaporate any of the three at any given time, as per Fig. 2a.

For LZ, in addition to the single 97 wt% $La_2Zr_2O_7$ + 3 wt% Y_2O_3 ingot method described above, additional samples were produced by evaporating one La_2O_3 ingot [manufactured by TCI Ceramics Inc., US] and one PYSZ ingot simultaneously, as illustrated in Fig. 2b, which will be referred to as co-evaporation in this paper. Co-evaporation is possible by creating a cycle in Von Ardenne's Beam Guidance software where first the electron beam is aimed at the PYSZ ingot and then quickly changed to target the lanthana ingot. The total cycle duration is of the order of tens of a millisecond, short enough that the untargeted ingot does not cool down and both ingots are simultaneously evaporating material. The ideal residence time on each ingot, referred to as "cycle split" in this paper, was not known so the deposition experiment trialled 4 different cycle splits. The optimum cycle split will be determined from the ease of evaporation and characterisation of the deposited coating.

The deposition conditions are listed below:

- Sample rotation speed: 8 rpm.
- Sample to ingot distance: 350 mm.
- Pressure: $5 \pm 1 \times 10^{-3}$ mbar, maintained by PID adding 90 % O_2 / 10 % Ar gas into the chamber as required in the range 100–700 sccm.
- Temperature setpoint of furnaces: 1030 °C.
- Average temperature of the substrates during deposition*:
  - PYSZ: 942 to 982 °C; interlayers: 945 to 995 °C.
  - GZ: 956 to 1008 °C.
  - NZ 4-layer: 961 to 975 °C and 964 to 994 °C; 2-layer: 922 to 968 °C.
  - LZ: 950 to 963 °C.
  - Co-deposited LZ: 958 to 995 °C.
- Power applied to ingots:
  - PYSZ: 26.5–28.2 kW.
  - GZ: 24.7–25.5 kW.
  - NZ 4-layer: 24.1–25.1 kW and 22.2–22.5 kW; 2-layer: 19.1–22.7 kW
  - LZ: 26.1–27.8 kW.
  - Co-deposited LZ: 33.0–40.0 kW.

* The average temperature of the substrates is inferred from temperature readings from a witness thermocouple during deposition and then corrected with data from a thermal calibration performed previously with UKAS calibrated thermocouples embedded into samples at the holder positions. During deposition, the temperature usually increases, so the minimum and maximum temperatures are reported.

2.2. Evaluation of manufacturability

This work considers the following factors to evaluate the manufacturability of REZ TBCs: the ability to evaporate the ingots and their technical difficulty (evaporability), the ability to produce a defined columnar structure (columnarity), and the stoichiometry of the resulting chemical composition and its homogeneity through the coating thickness (composition).

Evaporability is the most qualitative of the three factors, which considers:

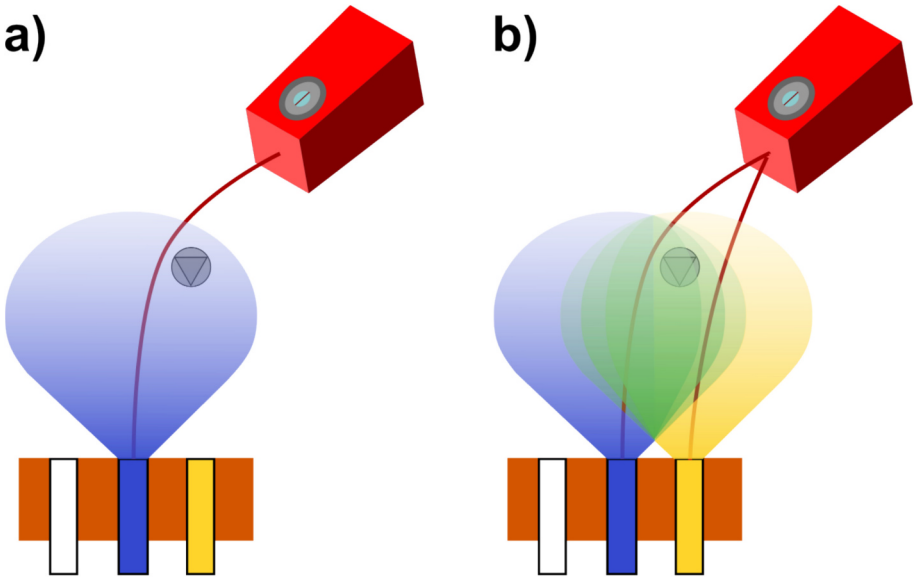


Fig. 2. Comparison of the distributions of the evaporation plumes of a) single-ingot evaporation and b) co-evaporation of two ingots, illustrated by different ingot colours.

- The formation of a coherent layer from the vapour phase that stays adhered to the substrate through light handling and testing.
- The shelf life of the precursor ingots.
- A subjective description of the amount of "spits" generated during deposition (droplets of molten material that escape from the melt pool at high velocities and land on the sample surface or elsewhere in the chamber).
- And a subjective description of the amount of ingot material molten but not evaporated during deposition. The unmolten ingot material concentrates around the edges of the ingot due to the cooler temperatures experienced by the contact with the cooled copper hearth, which can obstruct the formation of the plume, reduce sample temperature and block the operator's view of the melt pool that can result in an aborted deposition run.

Columnarity is somewhat qualitative too. The formation of defined columns has been assessed by visual inspection and classified as either columnar or not, including a brief description of the main traits of each columnar system.

2.3. CMAS testing

TBC samples were evenly covered in CMAS and exposed to a temperature above the CMAS melting point for short periods, aiming to capture the initial stages of reaction with the TBC and the formation of reaction layers and sealing phases, attempting to avoid the CMAS oversaturation of the TBC in isothermal conditions that would not be experienced in service.

The molar ratio of CMAS constituents used in this work is 35 % CaO + 10 % MgO + 7 % Al_2O_3 + 48 % SiO_2. A suspension was by magnetically stirring a 50:50 mixture (by volume) of CMAS powder and deionised water. The resulting suspension was applied using an air spray gun from a distance of 20 cm to the samples, which were pre-heated to quickly evaporate the water. Samples were weighed between spraying instances to ensure the CMAS loading on the sample surface was 15 ± 1 mg/cm^2.

CMAS-sprayed samples were introduced into a pre-heated furnace at 1300 °C for a controlled time of 30 min, timing from the moment the furnace recovered to 1295 °C, and cooled in air. Because of this high temperature exposure, the samples require the use of polycrystalline alumina substrates instead of a bondcoated Ni-alloy.

The evaluation of CMAS resistance was based on the extent of CMAS infiltration and the identification of reaction products on sample cross-sections inspected under Scanning Electron Microscope (SEM), detailed in Section 2.5.

2.4. Erosion testing

Erosion tests were performed at room temperature using the high-velocity erosion test facility at Cranfield University, thorough details on its principles of operation and characteristics can be found in a previous publication [14]. The erodent used was composed of angular alumina particles purchased from Guyson, UK (SaftiGrit White grade, Al_2O_3 content ~99.73 %) and then sieved to ensure a consistent particle size of 90–125 μm (i.e. the particles used could fit through a 125 μm sieve but not through a 90 μm sieve). Erodent was fed at a constant rate of 4.6 g/min, particles were accelerated to ~145 m/s (peak position of a velocity distribution of 134 particles measured by double-flash analysis by the National Physics Laboratory) in a tube 1 m long and 12.7 mm of bore and impacted the TBC samples at a standoff distance of 30 ± 2 mm and an angle of attack of 90° (i.e. direction of particles perpendicular to TBC surface), which results in a scar (area affected by erosion) roughly 20 mm in diameter.

TBC samples were regularly examined to quantify material loss, using repeat samples for each TBC material. At each interval, pictures were taken of the sample surfaces and samples were weighed using a precision balance (±0.1 mg). Inspection frequency was 30 s for 5 datapoints, increased to 60 s for at least 9 more datapoints, and further increased until TBC failure was achieved. TBC failure is defined as the first interval that displays a visible exposure of the bond coat.

The evaluation of erosion resistance in this paper is based on gravimetric data (i.e. mass loss), and the determination of erosion mechanisms is based on cross-sectional images obtained from eroded samples, the latter is described in Section 2.5. The gravimetric datapoints have been analysed following the procedure described in the ASTM G76–18 standard for erosion by solid particle impingement [15] (in particular, Fig. 5 and section 11.5 of the standard): datapoints arranged in scatterplots of sample mass loss vs accumulative erodent used, identification of linear region as the steady state and reporting of the steady state erosion rate (SSER) [16] as the slope of the linear region in both g/kg (g of coating loss / kg of erodent used) and mm^3/g (mm^3 of coating volume loss / g of erodent used). For the bilayer REZs, SSER only considers datapoints where the interlayer is not visible, as from that point onwards the mass loss depends on the resistance of both ceramic layers.

N.B. the testing reported in this paper does not comply with ASTM G76–18 due to larger erodent particle sizes, higher impact velocities, larger size of the erosion testing device, and testing of coating as opposed to bulk materials, but both methodologies follow the same testing and quantification principles.

2.5. Coating characterisation

Cross-sections of samples were obtained following typical metallographic preparation methods: cut with precision saw using an abrasive blade, mounted in conductive resin, ground with metallurgical grinding papers (120, 240, 1200 grit) and polished to mirror finish with diamond (6, 3 μm) and colloidal silica suspensions. Additional care was taken to preserve the damage inflicted from CMAS and erosion testing, tested samples were infused in protective resin before cutting with the precision saw.

Imaging was performed in SEMs at Cranfield University (Tescan Vega3, Vega4 and S8000) using the electron back-scattered detector. Representative images were taken of the as-deposited condition of all ceramic coatings as benchmark. For samples subjected to erosion testing, the cross-section was taken across the centre of the erosion scar. SEM images were taken starting at the edge of the scar and at known intervals from that reference point by keeping track of the X and Y positions of the moving stage. Thickness measurements were performed in comparable samples (produced in similar locations) and the result of 10 individual measurements in the software ImageJ.

Elemental analysis of the samples was performed by Energy Dispersive X-Ray Spectrometry (EDX) in the Tescan S8000 SEM. The distribution of the elements to quantify the homogeneity of the chemical composition of the coating and track the CMAS infiltration is based on linescans. All linescans presented in this work are constructed by post-processing EDX area maps of a width of ~280 μm and averaging each horizontal line of pixels using Aztec (Oxford Instruments) software, which gives a less localised measurement than a traditional linescan based on measuring a single line. The collective presence of Ca, Mg, Al and Si elements has been used to evaluate CMAS infiltration depth.

X-Ray Diffraction (XRD) was performed to determine the crystallographic structure of the as deposited coatings using a Siemens D5005 diffractometer using Cu Kα radiation at 20 kV at Cranfield University, from 10 to 90 2θ-angles with step size 0.4° and dwell 1 s.

3. Results

3.1. Manufacturability of rare-earth zirconate systems

The manufacturability of the REZ TBCs has been evaluated based on the three criteria described in Section 2.2: evaporability, columnarity and composition. Composition has been quantified using EDX linescans

as described in Section 2.5. Due to the lower accuracy of EDX in quantifying oxygen, the ratio between the two main metal constituents (Zr and either La, Gd or Nd) has been considered.

PYSZ has been deposited as a benchmark material. Its evaporability is excellent, achieving an adherent and resistant coating, experiencing low levels of "spits" and molten but unevaporated material. The composition achieved is very homogeneous through the 166 ± 1 μm of thickness, and it displays a very defined columnar structure with broad, non-branched columns (10 ± 3 μm-thick close to the surface, at a height or coating thickness value of ~150 μm) (Fig. 3).

3.1.1. Gadolinium zirconate

The gadolinium zirconate $Gd_2Zr_2O_7$ (GZ) showed good evaporability, producing thick adherent coatings, experiencing low levels of spits and of molten but unevaporated material, although in both cases slightly more than PYSZ. Molten but unevaporated remains of GZ were analysed by EDX, the Zr-to-Gd ratio was ~2-to-1.

The TBCs produced consisted of an initial interlayer of PYSZ of 24.5 ± 0.5 μm followed by a GZ top layer of 216 ± 2 μm (Fig. 4), with a defined columnar structure. In this case, it is worth noting that the GZ columns grow at a slight angle of ~15° with respect to the vertical PYSZ interlayer columns and that the GZ top layer columns branch out more than the usual monolithic PYSZ structure of Fig. 3, in general filling out the gaps trailing behind the off-normal column growth and leading to wider intercolumnar gaps in outer layers of GZ. Column inclination is consistent across different cross-sections and the component normal to Fig. 4 is negligible as observed in perpendicular cuts such as Fig. 9b.

The chemical composition of the GZ coatings was homogeneous through-thickness, slightly richer in Zr than stoichiometric (average Zr/Gd ratio of 1.10), although faint banding can be seen in the backscattered image and the EDX linescan confirms the Zr/Gd ratio oscillates between 0.90 and 1.32 (Fig. 4).

3.1.2. Neodymium zirconate

The EB-PVD deposition of the novel neodymium zirconate $Nd_2Zr_2O_7$ (NZ) proved successful and relatively straightforward. Because of the unfamiliarity of the NZ system, a first batch of samples was deposited following a four-layer design: a first layer of PYSZ (PZ1), a first layer of NZ (NZ1), a second layer of PYSZ (PZ2), and a second layer of NZ (NZ2) (see Fig. 5a). The PZ2 interlayer enabled a clear distinction of the effect of the different deposition parameters used for the two NZ layers. The NZ2 layer was too thin to provide reliable erosion data, so a second trial was set up following a bilayer design (see Fig. 5b) as described in the methodology, using the knowledge gained from the first trial.

The evaporability of the NZ system was also good, slightly inferior but comparable to GZ: both the 4-layer and 2-layer systems produced thick adherent coatings of blue colour, the deposition of NZ1 experienced severe cases of spits which were greatly mitigated in NZ2 and the second trial by using lower evaporation powers, ending up comparable to the GZ system. The 2-layer system consisted of an initial interlayer of PYSZ of 26.7 ± 1.0 μm followed by a NZ top layer of 169 ± 3 μm.

Both trials experienced significantly larger portions of molten but not evaporated material than for PYSZ or GZ, especially NZ2 and the last third of the second trial, possibly a consequence of the lower evaporation power. Unfortunately, the material was not quantified at the time but we recommend to weigh it in the future.

The NZ TBCs for both trials display a marked columnar structure with some degree of branching (Fig. 5a and b), similar to the GZ system (Fig. 4). Also like GZ, the columns seem to lean ~15° off the vertical for the TBCs from the first trial (Fig. 5a), especially evident for the NZ1 layer that is thicker (46.3 ± 0.8 μm) than the NZ2 layer (39.0 ± 1.1 μm), but some bending can be observed in the NZ2 layer too (Fig. 5b). The same inclination can be found in the second trial, while the normal component of this inclination is negligible as assessed in cross-sections perpendicular to the initial orientation (Fig. 5b). This alternative view highlights the branching especially on the outer third of the coating.

The backscattered images suggest a fairly uniform stoichiometry of the NZ layers with a few notable exceptions that are more Zr-rich: around the middle of NZ1 layer in the first trial ("A"), a region slightly past the first third of the second trial ("B") and for the whole last quarter of the second trial ("C"). The EDX linescan provides a more nuanced account of the Zr/Nd ratio, which is on average slightly richer in Nd than stoichiometric during the second trial (average Zr/Nd ratio of 0.88). Interestingly, the lower part of the NZ layer is stoichiometric $Nd_2Zr_2O_7$ (Zr/Nd ratio of 1.01), which is then slightly enriched in Nd (Zr/Nd = 0.79) until instance "B" is reached (Zr/Nd = 1.06) to continue with the enrichment in Nd until Zr/Nd = 0.68 (i.e. Zr/Nd ~2/3). After that, instance "C" is reached where there is a reversal and Zr/Nd

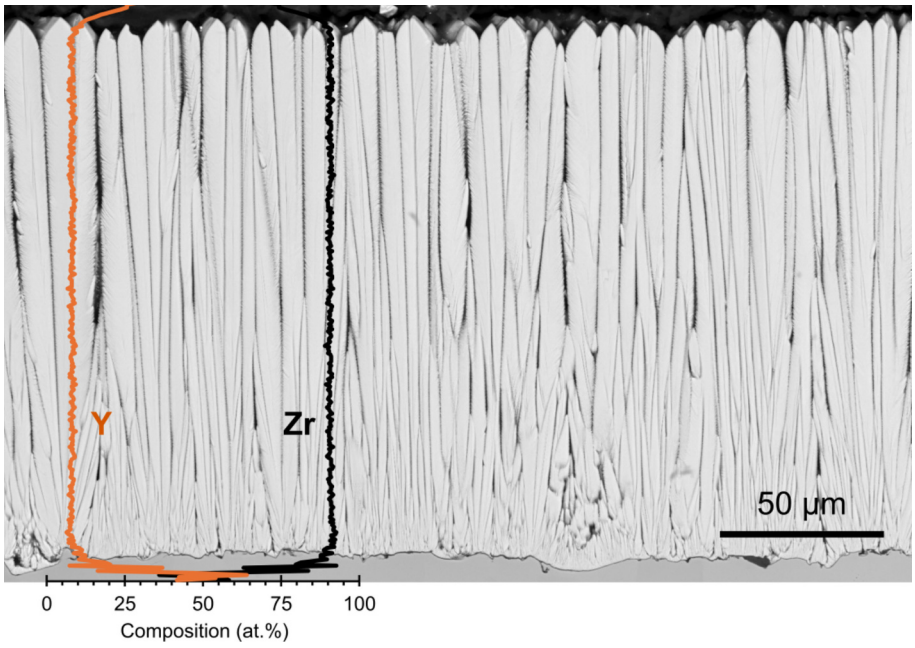


Fig. 3. Cross-section of PYSZ TBC on aluminised Nimonic 75 alloy in as-deposited condition taken with backscattered detector, overlayed with EDX linescan normalised to only include the metallic elements of the oxides (Y in orange and Zr in black).

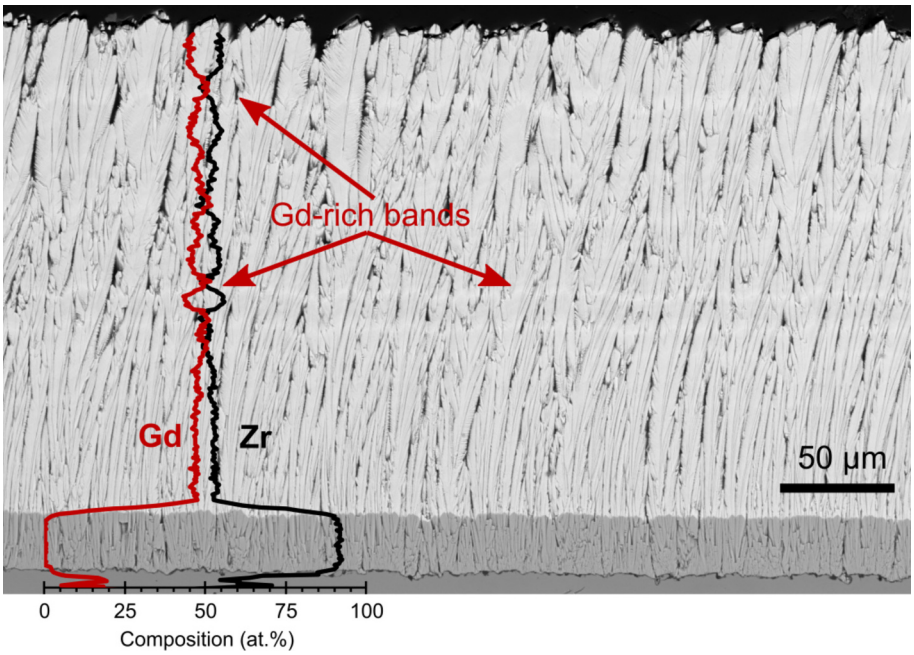


Fig. 4. Cross-section of gadolinium zirconate TBC on aluminised Nimonic 75 alloy in as-deposited condition taken with backscattered detector, overlayed with EDX linescan normalised to only include the metallic elements of the oxides (Gd in red, Zr in black, Y not plotted). Some Gd-rich banding is noticeable.

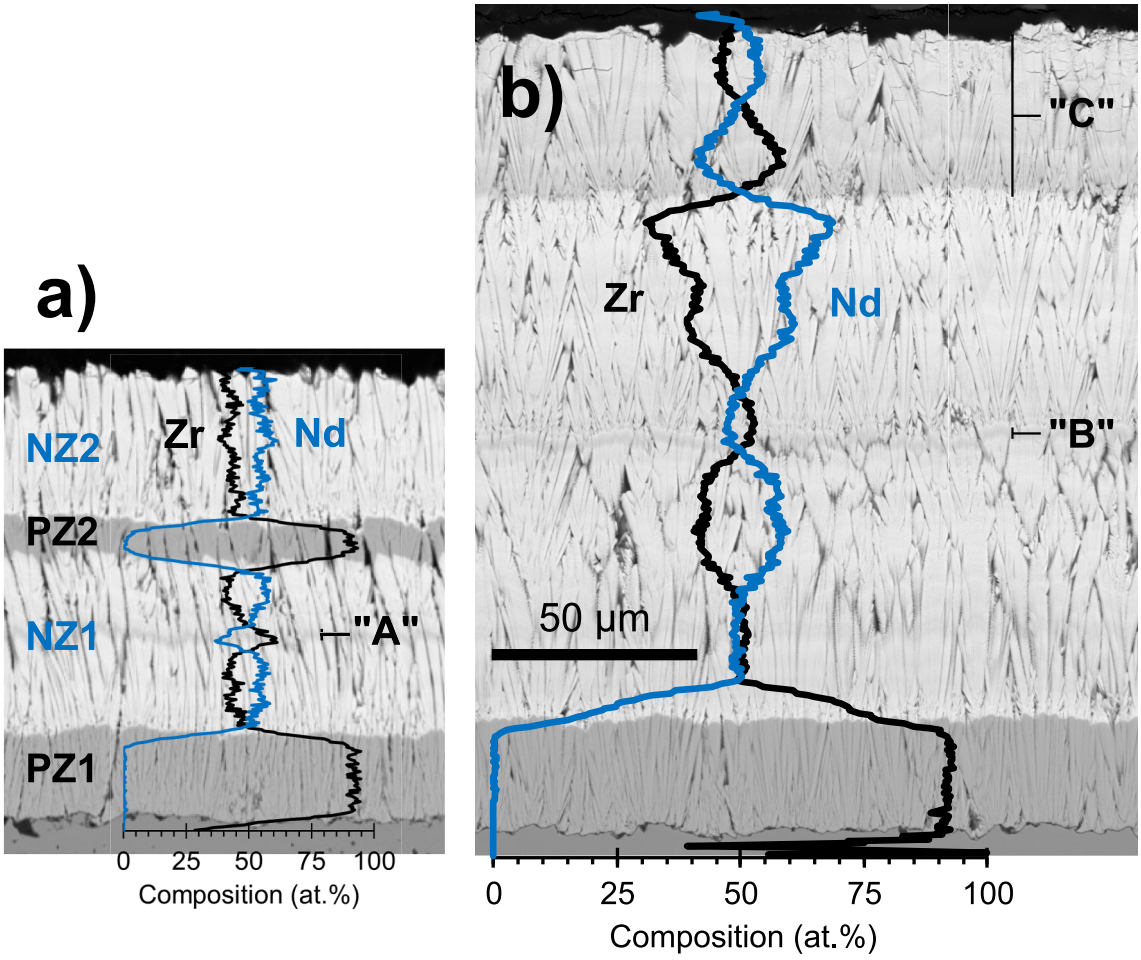


Fig. 5. Cross-section of neodymium zirconate TBC on aluminised Nimonic 75 alloy in as-deposited condition taken with backscattered detector, a) from 4-layer system and b) from 2-layer coating overlayed with EDX linescan normalised to only include the metallic elements of the oxides (Nd in blue, Zr in black, Y not plotted). Key regions have been highlighted and named by capital letters.

increases to 1.19, dropping again close to the surface to 0.88.

Assuming a constant deposition rate, the through-thickness location of those areas of interest roughly coincides with the following events recorded in time during the deposition:

- Instance "A" coincides with increased spitting.
- Instance "B" coincides with an unmolten piece of material falling into the meltpool and melting followed by increased spitting.
- Instance "C" coincides with large unmolten pieces of ingot being independently molten by using a second electron beam pattern overlapping with the pattern to melt the ingot through the last quarter of the deposition process, a longer event than the previous two that coincides with a thicker region.

3.1.3. Lanthanum zirconate

The lanthanum zirconate $La_2Zr_2O_7$ (LZ) from a single LZ ingot presented poor evaporability. A thick, adherent coating was achieved despite occasional spitting and significant amounts of molten but not evaporated material from the ingot were experienced in multiple coating attempts. In addition, the initial contact of the electron beam with the ingot tended to violently crack the ingot and eject material.

The LZ TBCs consisted of an initial interlayer of PYSZ of 17.3 ± 0.7 μm followed by a LZ top layer of 47.3 ± 1.0 μm (Fig. 6a), and additional deposition attempts yielded LZ top layer thicknesses of up to 100 μm. The LZ layer morphology lacked the clearly defined columnar structure of typical TBCs and varied greatly across the coating thickness. Starting with poorly defined, thin columns for less than the first half of the coating, the morphology transitioned to a fibrous structure, with evident composition banding both in the backscattered and EDX signal. The coatings deposited on bondcoated Nimonic 75 have slightly more defined columns than those deposited on alumina (Fig. 6b). Some vertical, through-thickness cracks are noticeable in the LZ layer.

The LZ coating composition oscillated around stoichiometric $La_2Zr_2O_7$ for the first ~20 μm, but it then became enriched in La for the following ~20 μm (Zr/La ratio of 0.33 to 0.67). The La-rich region coincides with the increased presence of unevaporated material around the meltpool, and it also displays a marked reduction in columnarity. Extremely La-rich bands are where the columnar structure disappears, to be re-nucleated in some cases in subsequent regions with lower La content. Unexpectedly, the trend reverses and $La_2Zr_2O_7$ stoichiometry is regained for the last 5–8 μm of the coating without apparent reason.

3.1.4. Co-evaporation of lanthana and PYSZ

The method of co-evaporation and terms described in this section are detailed in Section 2.1. The ideal cycle split between PYSZ and La_2O_3 was not known. To determine it, the deposition process of the co-evaporated LZ layer was divided into 4 sections with different beam residence times for the two materials and the amount of ingot consumed was recorded for each section, as summarised in Table 1. Sections 1 and 2 used a different La_2O_3 ingot than Sections 3 and 4 (the hearth can hold a total of 3 ingots) because of the short length of the available ingots, as they are difficult to manufacture. For the first ingot, the amount of material evaporated for both ingots is roughly the same. For the second ingot, there is an imbalance, with more lanthana evaporating than PYSZ.

Co-evaporation of LZ was successful and produced a very thick coating with reduced spitting and reduced unmolten ingot material leftover compared to single-ingot LZ evaporation; therefore, evaporability seemed to have improved. Most coatings were initially adhering, except some TBC spallation in a few aluminised Nimonic 75 samples. The spalled TBC remains were located close to the sample holder which, together with posterior desktop spallation of the aluminised Nimonic 75 samples, seems to indicate that spallation is caused by hydration of the LZ samples when exposed to atmosphere as opposed to poor adhesion. Desktop failure occurred on samples that withstood handling and were left unattended inside bags or on a table under ambient conditions. Attempts to preserve Nimonic 75 samples by infusing them with resin were unsuccessful; the coating fractured upon contact with the resin. TBCs on alumina disc substrates fared better, with several samples preserved by resin or in desiccator boxes, lasting long enough for CMAS

Table 1
Summary of residence time of the electron beam in fraction of the cycle and of material evaporation in length of ingot during co-evaporation experiment of LZ for both ingot materials.

	PYSZ ingot		La_2O_3 ingots	
Section of co-evaporation experiment	Beam residence time (fraction of cycle)	Ingot consumption (length)	Beam residence time (fraction of cycle)	Ingot consumption (length)
1	67 %	15 mm	33 %	15 mm
2	59 %	15 mm	41 %	15 mm
3	63 %	5 mm	37 %	12 mm
4	59 %	12 mm	41 %	27 mm

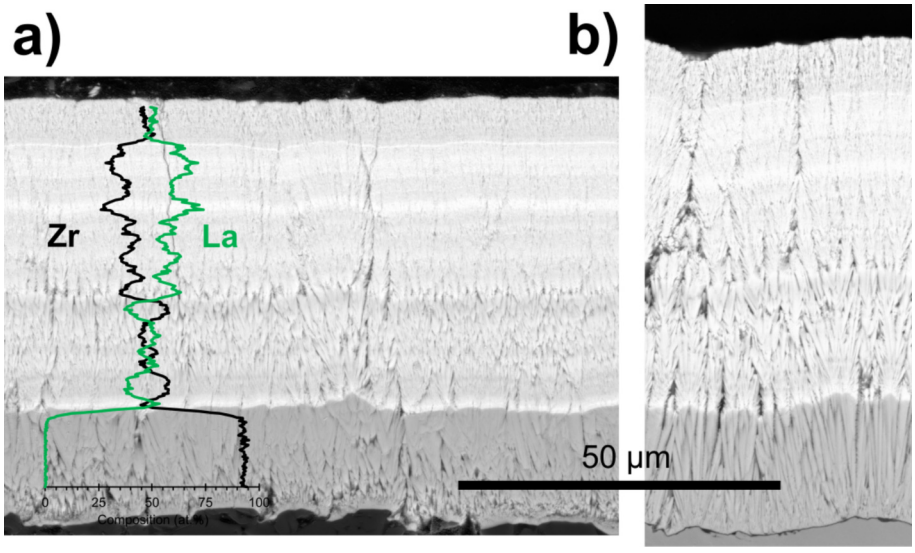


Fig. 6. Cross-section of lanthanum zirconate TBC in as-deposited condition taken with backscattered detector, a) on alumina substrate plus overlay of EDX linescan normalised to only include the metallic elements of the oxides (La in green, Zr in black, Y not plotted), and b) on aluminised Nimonic 75 alloy.

testing.

The La_2O_3 ingots were extremely hygroscopic, as expected. If ingots could be introduced into the chamber and immediately pumped, they could be used. Once unsealed from its plastic bag, one ingot was reduced to dust in around one hour, in stark contrast with the long shelf-lives of the other compounds, which are of at least 4 years for NZ and LZ (sealed in plastic; for which none have degraded since purchase) and decades for GZ and PYSZ.

The resulting coatings have a 39.0 ± 0.5 μm PYSZ interlayer and a 121.9 ± 0.8 μm thick LZ layer (Fig. 7). Four distinct regions can be identified in the LZ layer, which roughly correspond to the 4 sections of the deposition experiment (Table 1). Region I has some columnar traits, although fine and less defined, and has a constant Zr-rich stoichiometry (Zr/La of 1.38) without any banding. Regions II, III and IV are not columnar at all, with II and IV being markedly La-rich. The chemical composition is more homogeneous for all regions than in single-ingot evaporation of LZ, although some variability remains in regions II and III. XRD analysis from the surface of the LZ co-evaporated samples (typical X-ray penetration of the instrument for dense, high-atomic-number compounds is less than 10 μm, therefore Region IV) matches best with hydrated lanthanum oxide ($La(OH)_3$), although some peaks are still common to the very different spectra from the LZ TBCs evaporated from a single ingot and the LZ ingot itself (Fig. 8), which corroborates the hydration observed in desktop failures.

The crystalline structure of the LZ coating deposited from a single source shows peaks at ~26° and ~ 42° indicative of pyrochlore superlattice in LZ (which is more clear in the LZ ingot), as well as main double-peaks. On the other hand, the GZ spectrum matches the JCPDS card number 01–078-4083 corresponding to Fm-3 m space group (defective fluorite), while lacking pyrochlore superlattice peaks such as those observed in JCPDS card number 01–075-8269 corresponding to Fd-3 m space group. The NZ pattern also lacks the pyrochlore peaks and is similar to JCPDS card number 01–078-1289 (Fm-3 m).

3.2. CMAS resistance of rare-earth zirconate systems

Comparative CMAS resistance was evaluated for the four single-evaporated systems deposited on alumina substrates by exposing CMAS-covered samples to 1300 °C for 30 minutes.

PYSZ provides a benchmark performance. After exposure, PYSZ is fully infiltrated as attested by EDX and the formation of spherical globules at the base of the columns (Fig. 9a). Moreover, the morphology of the columns and internal porosity is severely affected due to interaction with CMAS.

GZ displays the best resistance to CMAS infiltration. A thin (3–5 μm) reaction layer forms that effectively blocks CMAS infiltration down the columns (Fig. 9b), after coating consumption of only 10–15 μm. A small amount of CMAS is detected below the reaction layer, probably due to infiltration while the reaction layer was forming. The morphology of the GZ columns has been preserved, except for consumption of the tips to the reaction layer. Note that the CMAS linescan has been constructed by adding the contributions of Ca, Mg, Al and Si and, therefore, the alumina substrate makes the CMAS proportion artificially surge at the bottom of the coating.

NZ also displays outstanding resistance to CMAS infiltration. A much thicker (~ 25 μm) reaction layer is formed than in the case of GZ, but the coating consumption is also small at 15–20 μm (Fig. 9c). The morphology of the NZ columns is perfectly preserved too.

Finally, the LZ system forms a reaction layer ~20 μm, similar to NZ in thickness but not in effectiveness, as CMAS seems to have penetrated through the whole LZ coating thickness (d). Inspection of wider sections of the coating revealed the periodic appearance of wide vertical cracks like that to the right of Fig. 9d, which act as conduits for CMAS infiltration. These are probably formed during the expansion of the coating when heating up, as the cracks are filled with molten CMAS but were not noticeable in the as-deposited condition. The faint columnar features of LZ have been completely lost and the morphology has significantly changed after CMAS infiltration.

3.3. Erosion resistance of rare-earth zirconate systems

Two samples of each TBC system produced from single-ingot evaporation were erosion tested (none of the co-evaporated LZ samples on aluminised Nimonic 75 survived). The variation of Steady-State Erosion

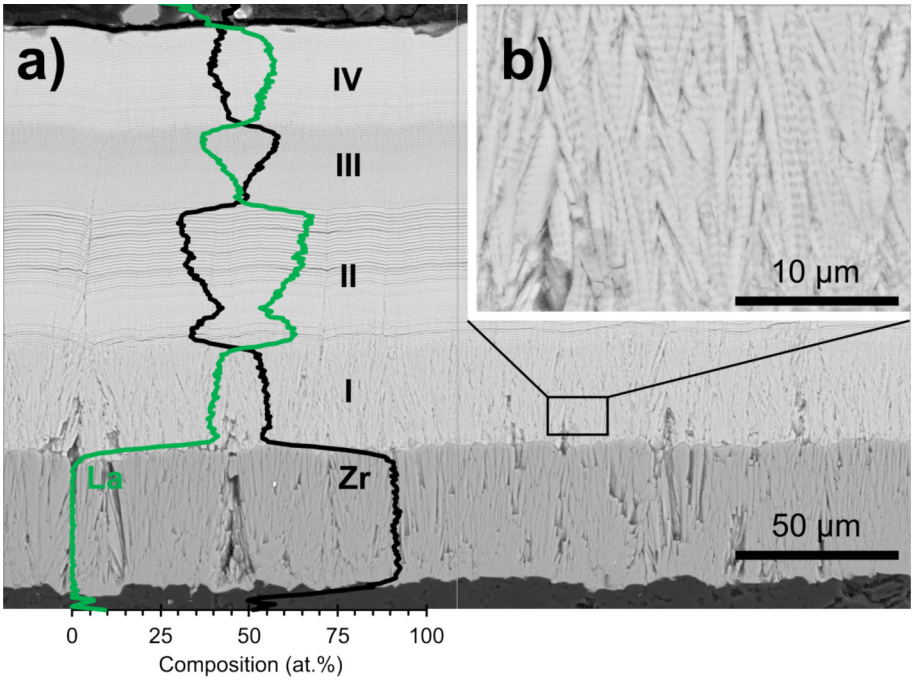


Fig. 7. Cross-section of lanthanum zirconate TBC on alumina, co-evaporated from LZ and PYSZ ingots, a) in as-deposited condition taken with backscattered detector overlayed with EDX linescan normalised to only include the metallic elements of the oxides (La in green, Zr in black, Y not plotted), presents four distinct Regions I-IV. b) Higher magnification of the lower region (I).

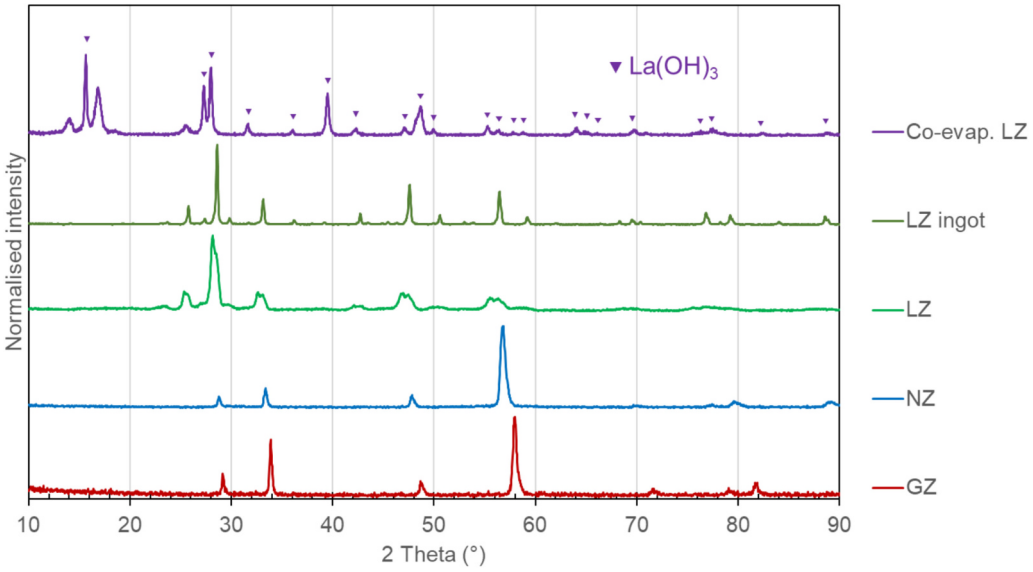


Fig. 8. XRD spectra obtained from the surface of co-evaporated LZ TBC, the LZ TBC produced from a single ingot, the LZ ingot, the NZ TBC and the GZ TBC.

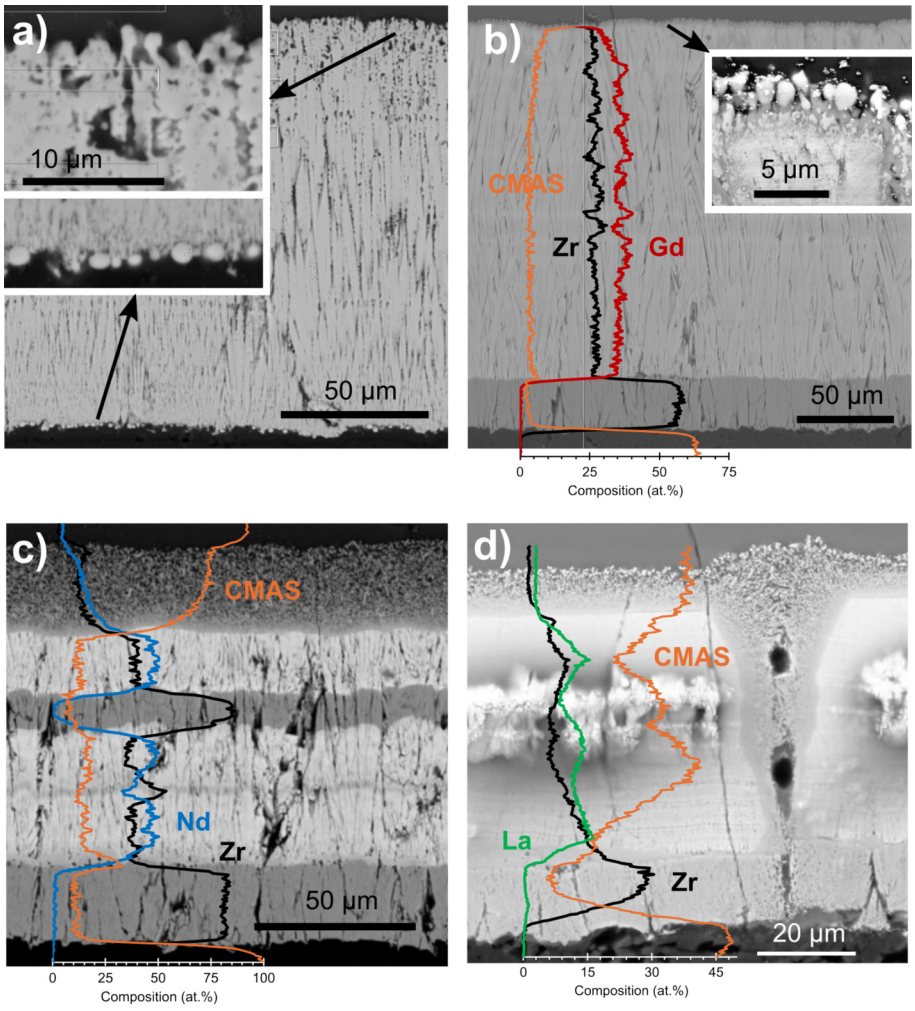


Fig. 9. Cross-section images of different TBCs after CMAS exposure for 30 min at 1300 °C taken with backscattered detector, overlayed with EDX linescan normalised to only include the metallic elements of the oxides. a) PYSZ, b) gadolinium zirconate, c) neodymium zirconate, d) lanthanum zirconate.

Rates (SSER, see Fig. 10) between the two samples of each system was very low for all columnar systems (~8 % for GZ and much lower for the rest), and higher at 15 % for the LZ system. PYSZ had the highest erosion resistance of all with an SSER of 4.9 g/kg or 0.8 mm^3/g (assuming bulk

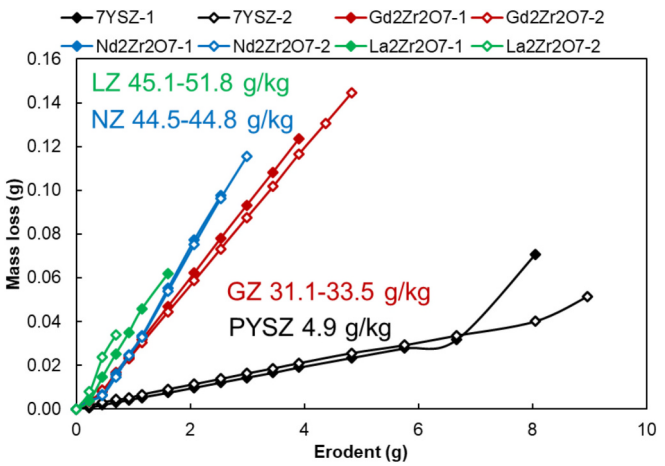


Fig. 10. Curves of mass loss vs erodent used during erosion testing of PYSZ, GZ, NZ and LZ coatings including their steady state erosion rate.

PYSZ density) for both samples, much lower than the REZ systems. GZ was the next best system for erosion resistance at 31.1 and 33.5 g/kg, or 4.9 and 5.3 mm^3/g, followed by NZ at 44.5 and 44.8 g/kg, or 7.4 and 7.5 mm^3/g. NB For NZ, the 2-layer design has been tested. It is worth noting that the NZ curve seems to have a lower slope below 1.15 g of erodent on the X-axis, but the SSER has been calculated using datapoints from both. Finally, the LZ system is the least erosion resistant at 45.1 and 51.8 g/kg, or 7.6 and 8.8 mm^3/g.

The erosion mechanism of the TBCs was identified via cross-section images taken across the erosion scar. For the columnar systems, horizontal cracks formed parallel to the coating surface, which eventually coalesce and lead to material removal. The PYSZ system has many unconnected cracks around the scar edge (Fig. 11, point "A"), which suggests cracks are formed by different impacts and, in general, do not propagate well across columns, although some degree of contiguous cracking just under the surface is observed in a few locations ("B").

The GZ coating, next best in erosion resistance, shows some degree of unconnected cracking away from the scar (Fig. 12, point "A"), but those cracks are of larger length than in PYSZ and often affect a few neighbouring columns ("B"). A significant number of contiguous cracks are found closer to the scar ("C"), which probably contributes to the increased rate of material removal.

The NZ system displays a similar cracking behaviour to GZ, with again some cracks affecting only a few columns (Fig. 13, point "A") but also with several contiguous, long cracks ("B"). The inhomogeneities in composition seen in the as-deposited condition (Fig. 5) seem to be affecting the erosion behaviour of the sample and leading to the formation of "rings" visible on the sample surface (Fig. 13, point "C"). These rings correspond to "steps" in the cross-sections that follow both the top, darker region of the coating ("D") and the band around halfway through the coating thickness ("E").

The LZ system displays the most widespread cracking systems due to the lack of a defined columnar structure (Fig. 14). The sample presented in Section 3.1.3 was relatively thin (LZ topcoat 47.3 ± 1.0 μm as per Fig. 6) and had the highest SSER of all (51.8 g/kg), although only a few datapoints were available for the calculation. In this sample, the cracking neatly follows the compositional banding, with the crack avoiding the tougher Zr-rich bands (Fig. 14a, point "A"). A second deposition was performed to obtain a thicker coating, which had an LZ topcoat thickness of ~100 μm (Fig. 14b). This sample withstood the test for twice as long (1.61 g vs 0.69 g of erodent at point of failure) so a more accurate SSER calculation could be performed (45.1 g/kg). The second sample behaves in the same way as the first, with the fibrous structure unable to stop crack propagation ("B").

4. Discussion

4.1. Challenges during deposition of REZ TBCs

The evaporation of the different REZ systems varied greatly: from the easy deposition for GZ, to some stoichiometry heterogeneity for NZ, to several issues achieving composition homogeneity and columnarity in LZ coatings. The results and observations during the deposition processes indicate possible root causes and offer valuable lessons for improving the manufacturability of REZ TBCs.

Among the three REZs tested, GZ demonstrated the best

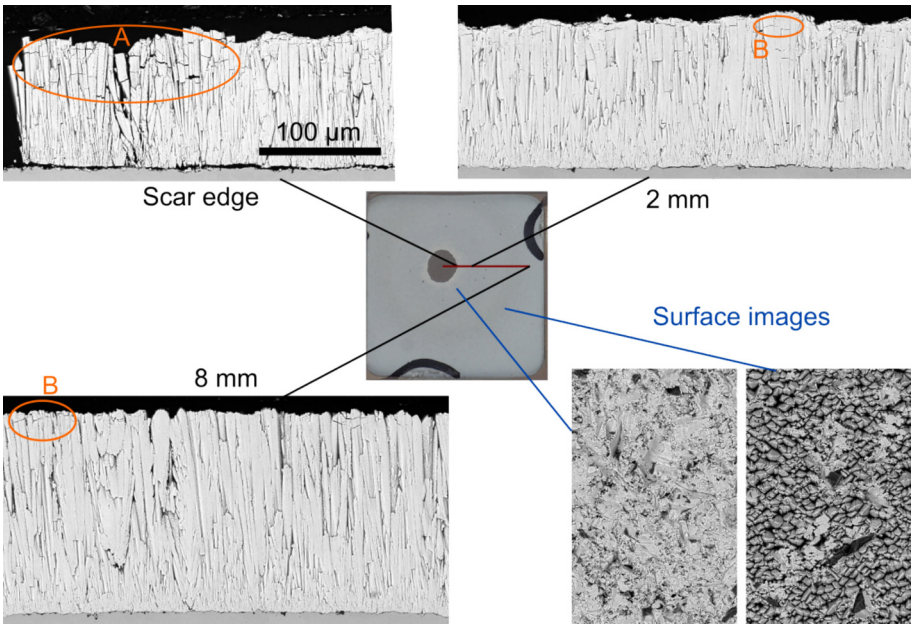


Fig. 11. Composite image of an eroded PYSZ TBC sample. The macroscopic optical image indicates the locations where cross-sections and surface images were taken with backscattered SEM detector (all at the same magnification). The reference positions of the cross-sections are related to the distance to the edge of the delaminated area (scar).

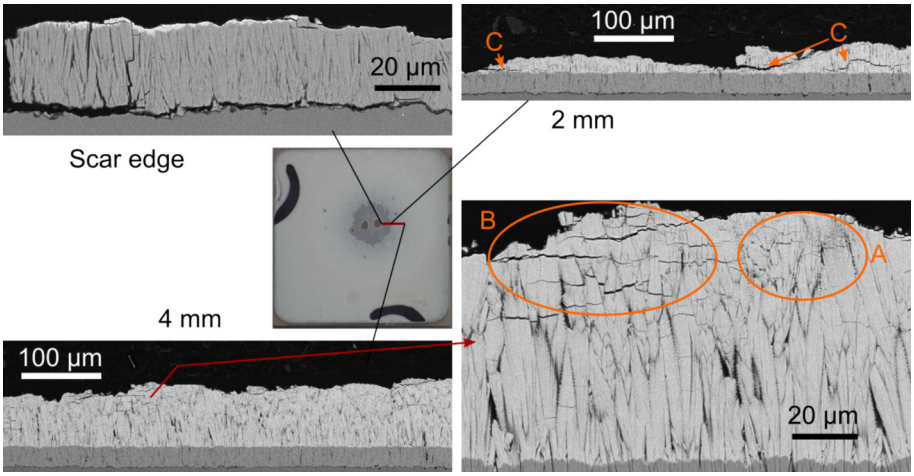


Fig. 12. Composite image of an eroded GZ TBC sample. The macroscopic optical image indicates the locations where cross-sections were taken with backscattered SEM detector. The reference positions of the cross-sections are related to the distance to the edge of the delaminated area (scar).

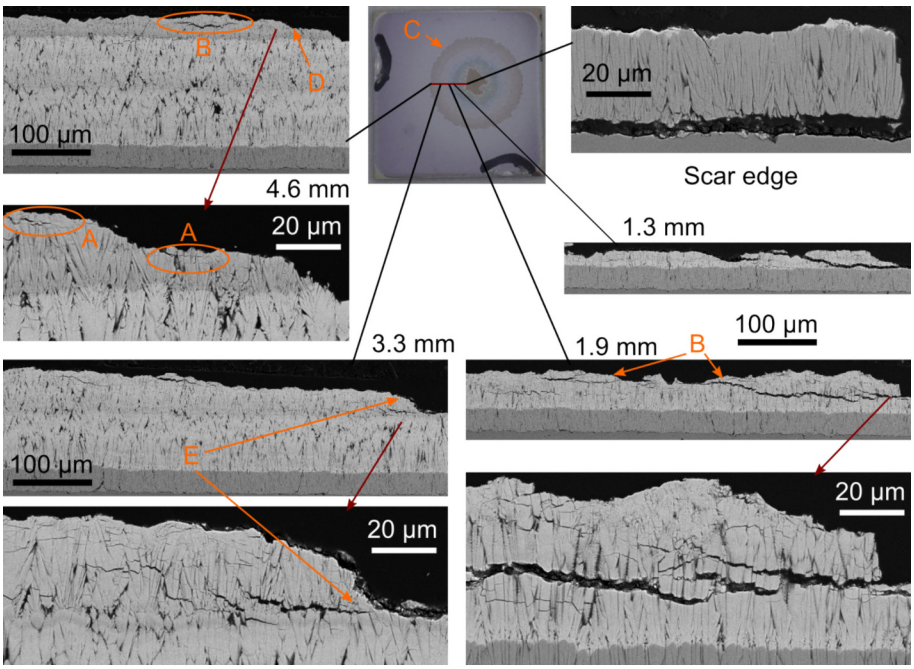


Fig. 13. Composite image of an eroded NZ TBC sample. The macroscopic optical image indicates the locations where cross-sections were taken with backscattered SEM detector. The reference positions of the cross-sections are related to the distance to the edge of the delaminated area (scar).

manufacturability as defined in this paper. The evaporability of GZ was the best of the REZs, with very little molten non-evaporated remains on the rim of the molten pool. We suggest weighing the amount of this material and normalising by the amount of ingot consumed (i.e. providing the ratio of molten non-evaporated vs evaporated) in future experiments to quantify this aspect of manufacturability. Unfortunately, the original set of experiments did not consider this approach, therefore the current assessment can only be qualitative. The elemental analysis of the molten but non-evaporated material showed a Zr/Gd ratio of ~2, proving the preferential evaporation of gadolinia, because of its higher partial pressure and in line with the results of previous simulations [17].

The columnarity of the coating morphology obtained is very well defined but subtly different from PYSZ columns: PYSZ are blocky and monolithic, while GZ columns are more branched out, as described in the present paper and explicitly noted previously in literature [13]. The community currently lacks a methodology or metrics to quantify these differences. A reduction in branching could be achieved by altering key process parameters, mainly temperature and rotation speed, possibly pressure, as they are known to have marked morphological effects [18,19]. Considering a recent DLR study with comparable deposition temperatures (930 to 1030 °C) [20], slightly increasing the deposition temperature of GZ to 1030 °C or increasing the rotation speed by ~66 % could reduce branching. It has been observed in the present study that GZO columns grow ~15° off-normal and that most branching appears to be filling out the space left by the bending, while branching is also contributing to wider intercolumnar spaces on the outer layers due to lower packing density of branched-off columns compared to monolithic PYSZ columns. Inclination has been observed in the literature before (Fig. 5 in [7]). It is suspected that the inclination of the columns is correlated with two factors: i) the direction of rotation of the samples during deposition, as the cross-sections in this work were taken either parallel or perpendicular to sample rotation, with one of the orientations resulting in negligible deviation from normal, and also observed in the literature [7,21]; and ii) change in preferential crystallographic

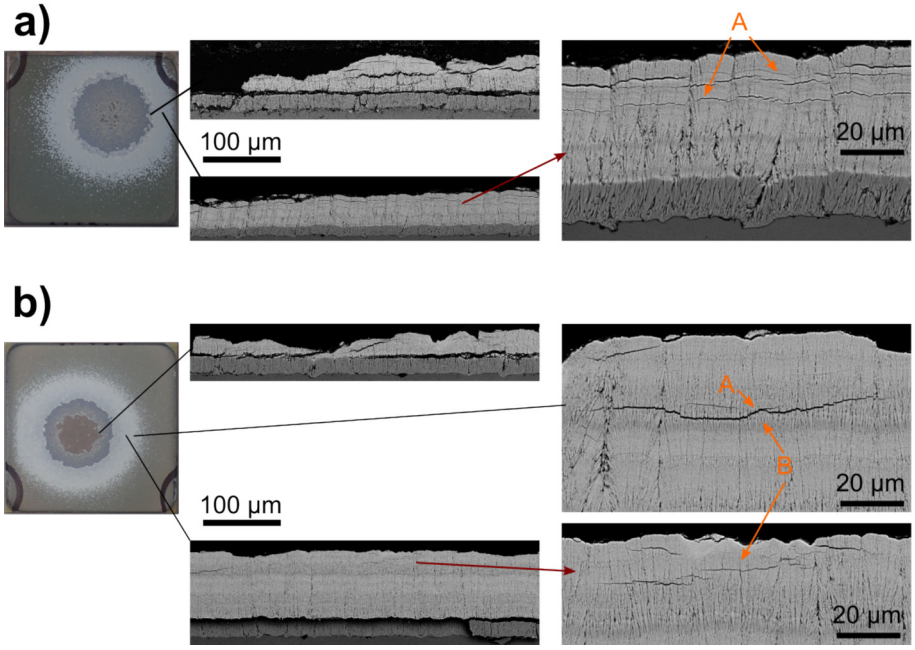


Fig. 14. Composite images of eroded LZ TBC samples. The macroscopic optical image indicates the locations where cross-sections were taken with backscattered SEM detector. a) is the lowest performing sample where extensive cracks appear located in composition bands, b) is the best performing LZ but extensive cracking is also noticeable.

orientation when transitioning from the t' PYSZ interlayer to the defective fluorite layer, like that observed in the cubic to t' transition in dysprosia-stabilised zirconia [21]. Other deposition parameters have not been explored in this work, but a previous studies has not seen correlation between temperature and inclination [20]. Regarding the crystalline structure of GZ, the key difference between a defective fluorite and fully ordered pyrochlore is usually identified by the detection of weak superlattice reflections [22,23], which have been reported for GZ at ~14°, 27°, 37°, 45° or 52° [24]. Those weak peaks are not present in the as-deposited GZ coating, indicating defective fluorite as the most likely structure (space group Fm-3 m), but we have observed in unpublished works that they transform to Fd-3 m (ordered pyrochlore) after exposure at high temperature (100 h at 1300 °C or above). This behaviour has been reported before by DLR, fluorite as-deposited [20,21] transforming to pyrochlore after ~2800 h at 1100 °C [21]. All in all, the GZ coatings obtained reflect the high degree of optimisation of the EB-PVD process with this material, a mature TBC system first produced by EB-PVD in experiments associated with patents from the early 2000s [1].

By contrast, the NZ system has not been extensively researched until now and, to the best of the authors' knowledge, the EB-PVD deposition of NZ has not been published before the current paper. Early work on the pyrochlore family included studies on NZ in pellet form [3], which revealed a promising performance of the material as TBC: with similar thermal conductivity to GZ (identical at 700 °C), while having a lower density and a much higher potential "maximum use temperature" based on the stability of a single phase (1575 °C for GZ compared to 2300 °C for NZ) than GZ. The current paper indicates the potential of NZ to achieve good manufacturability if the deposition process can be optimised. Despite its novelty, the evaporability of NZ was good, except for the three issues described in Section 3.1.2. In particular, the solidification of molten non-evaporated material around the meltpool has been the main cause of the inhomogeneities in composition seen in Fig. 5b. This material was not analysed on this occasion, but it is likely rich in Zr as per the GZ observations because of neodymia's higher vapour pressure. Pieces of this non-evaporated ingot falling into the meltpool, as well as the selective evaporation at later stages of the deposition process, increased the Zr content of those regions. If the process could be optimised, e.g. with the selection of an ideal evaporation power and electron-beam pattern, it is likely that these inhomogeneities can be reduced to GZ levels. Regarding columnarity, NZ seems to naturally form defined columns very similar to those of GZ, which suggests that column branching could be a feature associated with the deposition. As with GZ, NZ deposition may benefit from increased temperatures to reduce branching. The similarities between the two systems continue, with NZ also lacking weak superlattice peaks that suggest a defective fluorite crystalline structure.

The LZ system was one of the first rare-earth zirconates to gather attention and be deposited by EB-PVD due to its high thermal stability, resistance to sintering and potential resistance to CMAS. Since the first trial by the team at Cologne in 2004 [9], and through subsequent publications by them [10] and other groups [12], the deposition of LZ by EB-PVD has always been characterised by compositional heterogeneity and a lack of defined columnar structure. The EDX analysis overlayed on the backscattered image in Fig. 6 highlighted how the region where Zr/La ratio is around 1 (i.e. hovering around stoichiometric $La_2Zr_2O_7$) has some faint columnarity, whereas the outer regions are richer in La and completely lose the columns. The La-enrichment of later stages of the deposition can be explained by the large amount of molten but not evaporated material that solidified outside the meltpool, which is likely richer in Zr because of the same reasons explained for GZ and LZ and reported in $Sm_2Zr_2O_7$ by Kember [25], trapping therefore a large quantity of Zr that cannot be incorporated in the coating. An accurate measure of the leftover, molten but not evaporated, material will be required in the future to validate this observation. The amount of unevaporated material could be reduced by optimising the EB-PVD process for LZ; however, even in the "stoichiometric" region, the LZ system shows much more acute banding in the through-thickness composition than the other REZs, which is probably related to lanthana having the highest vapour pressure of all measured RE oxides [26] (and thus being farthest from zirconia). The role of partial pressure, initially suggested in the initial LZ paper [9], is supported by the predictions of the author's previous EB-PVD evaporation model [17] where lanthana was the oxide displaying more acute banding of all the tabulated oxides in [26]. This is also supported by the reported depletion of Sm on remnants of $Sm_2Zr_2O_7$ ingots after evaporation from Kember's MSc thesis [25].

To mitigate the banding, a small amount of Y_2O_3 was added into the ingots (3 wt%, see Section 2.1 for their composition) following initial suggestions [9] of its role as a moderator for the evaporation, but this strategy was not sufficient in completely avoiding banding in the original paper nor in the present work. Then, co-evaporation was examined, without much overall success either but for different reasons. On the one hand, banding has been mitigated by co-evaporation in all regions of Fig. 7 contrasting to single-ingot evaporation in Fig. 6, and specifically regions I and IV show a very homogeneous through-thickness stoichiometry. This experiment proves the suspicion that banding is caused by different partial pressures of species sharing a meltpool, as banding is not observed when the same oxides are evaporated separately, indicating that co-evaporation can be a successful strategy to obtain more homogeneous through-thickness compositions such as that of region I. On the other hand, the co-evaporated LZ coatings spalled and the handling of the La_2O_3 ingots proved impractical, all of which is caused by the known tendency of lanthana to form a hydroxide $La(OH)_3$ by hydration in regular atmospheric conditions. The excess of La on regions II, III and IV of the co-evaporated coating (Fig. 7) has extended this hydration tendency to the produced coatings, as demonstrated by the overwhelming presence of $La(OH)_3$ in XRD patterns (Fig. 8). This, together with the spalled coating debris located close to the sample holders (away from the plume) and the recorded desktop failures, all suggest coating spallation is caused by re-hydration upon/after venting the chamber rather than poor adhesion to the interlayer. Finally, LZ is the only system that presents weak peaks indicating a likely pyrochlore structure, which is different from the fluorite structure reported in the first EB-PVD LZ publication [9]. In that work, the main double-peaks were reported at the surface of one LZ coating, which was attributed to texturing.

In summary, co-evaporation may have some merit in reducing compositional banding when used with a less hygroscopic system. Reducing La content to sub-stoichiometric levels may reduce the hygroscopy of the resulting coating (although not of the precursor ingot) and perhaps transition to a more columnar microstructure, as in the study where this was trialled in the GZ system [13]. Exploring a wider range of deposition parameters could also change the morphology of the columns, as it is widely known [19,27,28], although our preliminary attempts to increase the deposition temperature were not effective in creating more defined LZ columns. Co-evaporation, a technique widely used in sputtering and in other EB-PVD studies to generate different ceramic stoichiometries [13], proved successful in obtaining homogeneous through-thickness compositions. However, two main limitations need to be considered i) First, the different sample-to-plume distances caused by the evaporation of two different ingots can cause compositional variation between samples produced in the same batch of coatings. ii) Second, the range of coating compositions that can be achieved with this technique is limited; extreme cases where the desired amount of the second material would be at low dopant levels, possibly in solid solution, cannot be achieved because there is a minimum residence time needed to evaporate the ingot, thus the cycle splits cannot cover the full range from 0 to 100 %.

4.2. Resistance to CMAS infiltration of REZ TBCs

Resistance to CMAS, together with lower thermal conductivity, is a key argument for proposing REZs as replacement materials for PYSZ-based TBCs. The present work shows the effectiveness of columnar REZs to block CMAS penetration by forming a reaction layer, in particular GZ and NZ. The lack of infiltration has been confirmed by visual changes in coating morphology and by tracking the presence of Ca, Mg, Al and Si elements by EDX linescans composed by aggregating data over regions ~280 μm wide. On the other hand, PYSZ is unable to form a dense reactive layer, hence it is fully infiltrated after only 30 min at 1300 °C. LZ is also unable to stop full infiltration, but for a different reason: the formation of vertical cracks during sample heating, likely a consequence of the thermal shock driven by the small difference between the coefficients of thermal expansion of the alumina substrate (around 8.5×10^{-6} K^{-1} [29] but can vary depending on purity) and LZ (9.1×10^{-6} K^{-1} [30]) and the lower strain compliance of the non-columnar morphology seen in the as-deposited condition (Fig. 6), as the reaction layer is fully formed in the TBC surface and around the crack. This observation seems supported by a previous study by Schultz and Braue [10], where the LZ TBC effectively blocked infiltration when no vertical cracks were generated. The observed differences likely arise from the different CMAS testing methodology used, as the team in Cologne loaded the samples in a cold furnace and slowly increased the temperature at 10 °C/min to 1260 °C, minimising thermal shock during heating, whereas the current study favoured shortening the residence time at lower temperatures and thus samples were loaded in a furnace already at 1300 °C. The present methodology favours observation of rapid reactions at the target temperature and avoids residence at intermediate temperatures, to the detriment of sample integrity for coatings that are not columnar and are sensitive to strain compliance or thermal shock. Despite the different methodologies, the surface reaction layer is morphologically very similar to Fig. 9d, a sign that the underlying mechanisms of reaction layer formation are the same.

The mechanism by which REZs prevent CMAS infiltration was identified by earlier works in Santa Barbara [6]: initial dissolution of the GZ leads to the formation of a reaction layer of globular fluorite (ZrO_2 with solid solution of Ca and Gd) plus needle-like apatite ($Gd_8Ca_2(SiO_6)_4O_2$) crystalline phases that block the channels between the EB-PVD columns. In the present study, the same phases and a thinner reaction layer (3–5 vs. 6 μm) have been formed in GZ exposed for shorter times (30 min vs. 4 h) at the same temperature. The present study highlights that, while the mechanism remains the same, the kinetics may change because different REs produce reaction layers of varying thicknesses (La ~20 μm, Nd ~25 μm, Gd ~3–5 μm). Similarly, this has also been observed by Ball et al. [31], who recently investigated Yb, Er, Gd and Sm zirconates in pellet form. Their conclusion from studying the enthalpy of formation of reaction phases is that apatite formation is faster for REs with increasing ionic radius, leading to a thicker reaction layer in elements to the left of the lanthanide series. The present paper confirms this trend for NZ and GZ but, at first glance, LZ seems not to follow this rule. This apparent incongruency is explained by the lack of columnarity of LZ, which reduces the coating surface area exposed to the molten CMAS and therefore limits the availability of coating material to diffuse into the CMAS and react. This agrees with the observation at Manchester [31] that diffusion rates in pellet form were much slower than in EB-PVD morphologies from previous studies, which again highlights the importance of coating morphology and the size of its features for CMAS resistance. Ball et al. [31] also posit that "the most optimal material for CMAS resistance would be whichever produces a dense barrier layer with the RE element of minimal RE ionic radius". The relatively short exposure (30 min) used in the current paper is insufficient to estimate the long-term loss of material under CMAS attack. Calculations of material loss for GZ and NZ (10–15 μm and 15–20 μm, respectively) are broadly in agreement with the previous premise, but the small difference might be affected by the use of different samples to estimate the coating thickness before and after CMAS exposure. In conclusion, the new NZ system seems to perform in a similar way to the GZ system in preventing CMAS infiltration, while the lack of columnarity of the LZ system has highlighted the influence of morphology can have on CMAS resistance.

4.3. Erosion mechanisms and performance of REZ TBCs

The main drawback of the REZs as PYSZ replacements is their lower fracture toughness, which leads to increased coating loss by solid particle erosion. As expected, the results in Fig. 10 highlight a significant difference between the coating families: the rate of material loss of PYSZ was between 6.4 and 10.6 times lower than that of REZs. Differences in

density of the different materials are small (ranging from 5.89 g/cm^3 of LZ to 6.32 g/cm^3 of GZ), but even accounting for this, the volume loss of REZs is over 6 times larger than that of PYSZ. Among REZs, GZ is the best-performing, with NZ having an erosion rate ~ 40 % higher in mass and volume, while LZ is ~60 % higher than GZ. LZ also displays larger variability, perhaps a consequence of the lack of a defined columnar structure of the system.

These results are in line with previous studies on erosion of PYSZ and GZ for SPS coatings [32] from Mahade et al. (although in that case erosion resistance of PYSZ was only twice that of GZ), and for EB-PVD coatings by Schmitt et al. [13]. The latter work found a difference between RE-doped PYSZ and GZ EB-PVD TBCs of one order of magnitude, and interestingly also included erosion results for intermediate stoichiometries. The researchers from Pennsylvania and Ohio correlated the increasing erosion rates to the different phases of the resulting coatings: from the ferroelastic toughening mechanism of the t' phase that confers the best performance to PYSZ, to a lower toughness of the cubic phase of intermediate stoichiometries, until the lowest erosion resistance of the pyrochlore. Therefore, the intrinsic toughness of the TBC material and its phase play a major role in explaining the erosion resistance of the systems tested in the present work. However, another very important factor is required to fully explain the differences between the REZ systems in the current work, and between the current work and previous works: coating morphology. The same study by Schmitt et al. [13] also tested pellets of the same compositions as the coatings, finding that the fracture resistance of PYSZ was only 3 times larger than GZ (not 10), and that the differences in erosion resistance of intermediate stoichiometries were of 33 % increase for pellets instead of 78 % for coatings. Despite the lack of images of the erosion damage from [13], the differences between pellets and EB-PVD coatings can be attributed to differences in coating morphology and texture observed in the various as-deposited conditions.

In the present work, additional focus has been put on identifying the erosion mechanisms of the different systems. PYSZ presents the classical material removal mechanism described almost three decades ago [14]: near-surface cracking is formed by individual impacts, but cracks do not propagate well into nearby columns in the EB-PVD structure; material removal happens when enough neighbouring columns have been cracked. The space between columns is an effective feature in stopping crack propagation as attested by the inferior erosion resistance of APS coatings that lack columnar structure [33], the increase in erosion resistance by decreasing column width in EB-PVD coatings [34], and by the increased erosion resistance of APS systems with induced vertical cracking [34]. The GZ and NZ coatings display the same material removal mechanism as PYSZ, with the difference that their column morphology appears less effective in stopping crack propagation: images from regions on the exterior of the erosion scar (therefore impacted by fewer particles than in the central region) in Fig. 12 and Fig. 13 show several contiguous cracks affecting multiple columns, which is less prominent for PYSZ in Fig. 11; in the central region, large contiguous cracks are visible for GZ and NZ but absent for PYSZ. This lower effectiveness could be explained by a combination of the lower toughness of the column material, together with some morphological factor. The ~15° inclination from the vertical consistently found in GZ and NZ columns may be playing a role here, as it is a known factor that deviation from normal to the substrate decreases erosion resistance [34], however this influence cannot be quantitatively assessed in the absence of non-inclined columns of the same material. Another factor may be the morphology of the columns, as GZ and NZ columns seem to branch out in contrast to the monolithic appearance of PYSZ columns. Perhaps the branching is a feature that concentrates tensions in the columns and/or transfers impact energy into adjacent columns, but this could not be assessed in this qualitative work. Currently, the community has noticed those morphological differences, e.g. in the description of the as-deposited conditions of GZ in [13], but it lacks a methodology or tool to quantify this qualitative assessment. Simple column counting is not enough to capture the subtlety of branching, as in general it is limited to a single measurement [35] while it is clear that column size changes with thickness. The case of LZ TBC is perhaps even more extreme, as the lack of a defined columnar structure seems to be very beneficial to crack propagation (no disruptive transverse interfaces) and explains the poor erosion results. Finally, the inhomogeneities in the composition of the NZ and LZ coatings seem to channel crack propagation towards regions with lower toughness and to produce step-like profiles on the erosion scar, as opposed to the smooth scar parabolic surface of homogeneous systems like PYSZ and GZ. The step-like profiles enable shear-like forces to be exerted on the column tips and increase material removal.

In summary, the current study has highlighted the importance of coating morphology in erosion resistance. Further understanding and quantification of the REZ coating morphology is necessary provide a strategy to improve their erosion resistance, as the differences in intrinsic properties with PYSZ seem to be smaller than the differences in erosion resistance. For the NZ system, improvements in coating homogeneity through deposition optimisation could improve erosion resistance, potentially equating that of GZ.

5. Conclusions

The manufacturability of PYSZ and three rare-earth zirconate TBC systems (gadolinium, neodymium and lanthanum zirconate) has been evaluated by assessing their evaporability, columnarity and composition homogeneity. For the first time, NZ TBCs were produced by EB-PVD and achieved good evaporability and defined columnarity, similar to GZ. The columns of NZ and GZ have a common morphology, branching out more than the monolithic PYSZ columns, which creates larger inter-columnar gaps in outer sections of the coating, and deviating ~15° from the vertical. Localised banding on the NZ TBCS was attributed to molten but not evaporated material, which could be reduced by optimising the deposition process, potentially achieving the same level of homogeneity as GZ.

LZ, on the other hand, presented high levels of non-evaporated ingot material that may contribute to the composition deviating from stoichiometric $La_2Zr_2O_7$ (enriched in La) at later stages of the deposition process. The La-enriched region is fibrous in morphology and lacks columnarity. Both the La-rich and the stoichiometric regions suffer from significant compositional banding despite the addition of Y_2O_3 as moderator, caused by differences in the partial pressure of La_2O_3 and ZrO_2. The co-evaporation of La_2O_3 and PYSZ ingots is effective at producing homogeneous through-thickness compositions on the resulting coatings; but, unfortunately, the La-rich resulting coating and the hygroscopic nature of La_2O_3 caused coating delamination by the formation of $La(OH)_3$.

Both GZ and NZ are effective at blocking CMAS infiltration and their morphologies are not negatively affected after 30 min at 1300 °C, conditions that completely flood and alter the morphology of PYSZ. The stopping mechanism is the quick formation of a reaction layer (3–5 μm for GZ and ~ 25 μm for NZ) via dissolution of small portions of the coating thickness (10–15 μm for GZ and 15–20 μm for NZ). By contrast, the lack of a defined columnar structure for the LZ coatings reduced their surface exposed to CMAS, reducing coating dissolution and producing a thinner reaction layer than expected (20 μm instead of thicker than NZ's), but at the cost of generating periodic vertical cracks during heating up, which allowed for CMAS infiltration through the coating thickness and thoroughly altered the morphology of the coating.

GZ is the most erosion-resistant of the REZ TBCs, although still loses 6 time more material than PYSZ under the same conditions. NZ erodes at a rate 40 % faster than GZ, but is negatively affected by the localised inhomogeneities of the through-thickness composition by forming vertical scar fronts and concentrating crack propagation. An optimised NZ coating is anticipated to increase its erosion resistance, possibly to levels similar to GZ. LZ lacks columnar structure and is the worst-performing coating with up to 60 % higher rate of material loss than GZ. This,

together with the smaller intrinsic difference in erosion resistance of fully dense REZ vs PYSZ, highlights the importance of coating morphology. Furthermore, incipient cracking within REZ eroded samples propagates through columns more than in PYSZ. A potential strategy to increase REZ resistance to erosion could be to alter the REZ column morphology to make the column boundaries so formed more effective in stopping crack propagation.

CRediT authorship contribution statement

Luis Isern: Writing – original draft, Visualization, Validation, Methodology, Investigation, Formal analysis, Data curation, Conceptualization. **Koldo Almandoz Forcen:** Writing – review & editing, Validation, Methodology, Investigation, Formal analysis, Data curation. **Christine Chalk:** Writing – review & editing, Supervision, Project administration, Methodology, Investigation, Funding acquisition, Formal analysis. **Gyaneshwara Brewster:** Writing – review & editing, Supervision, Resources, Methodology, Funding acquisition, Formal analysis. **Alan Johnstone:** Supervision, Resources, Funding acquisition. **John Nicholls:** Writing – review & editing, Supervision, Project administration, Methodology, Funding acquisition.

Funding sources

The authors are thankful to Innovate UK for their Smart Award project #10020751, “High temperature tools for designing sustainable erosion resistant coatings”, which partially funded this work, and to Rolls-Royce Plc for providing additional funds.

Declaration of competing interest

The authors declare the following financial interests/personal relationships which may be considered as potential competing interests: Luis Isern Arrom reports financial support was provided by Innovate UK. Luis Isern Arrom reports a relationship with Cranfield University that includes: employment. If there are other authors, they declare that they have no known competing financial interests or personal relationships that could have appeared to influence the work reported in this paper.

Acknowledgements

Dr. Tracey Roberts from Cranfield University is greatly acknowledged for her technical assistance in metallographic preparation of all samples.

Data availability

Data will be made available on request.

References

[1] M.J. Maloney, US Patent 6,284,323 B1, 2001.
[2] R. Vassen, X. Cao, F. Tietz, D. Basu, D. Stöver, Zirconates as new materials for thermal barrier coatings, J. Am. Ceram. Soc. 83 (2000) 2023–2028, https://doi.org/10.1111/j.1151-2916.2000.tb01506.x.
[3] J. Wu, X. Wei, N.P. Padture, P.G. Klemens, M. Gell, E. García, P. Miranzo, M. I. Osendi, Low-thermal-conductivity rare-earth zirconates for potential thermal-barrier-coating applications, J. Am. Ceram. Soc. 85 (2002) 3031–3035, https://doi.org/10.1111/j.1151-2916.2002.tb00574.x.
[4] E.M. Zaleski, C. Ensslen, C.G. Levi, Melting and crystallization of silicate systems relevant to thermal barrier coating damage, J. Am. Ceram. Soc. 98 (2015) 1642–1649, https://doi.org/10.1111/jace.13478.
[5] D.L. Poerschke, T.L. Barth, C.G. Levi, Equilibrium relationships between thermal barrier oxides and silicate melts, Acta Mater. 120 (2016) 302–314, https://doi.org/10.1016/j.actamat.2016.08.077.
[6] S. Krämer, J. Yang, C.G. Levi, Infiltration-inhibiting reaction of gadolinium zirconate thermal barrier coatings with CMAS melts, J. Am. Ceram. Soc. 91 (2008) 576–583, https://doi.org/10.1111/j.1551-2916.2007.02175.x.
[7] U. Schulz, A. Nowotnik, S. Kunkel, G. Reiter, Effect of processing and interface on the durability of single and bilayer 7YSZ / gadolinium zirconate EB-PVD thermal barrier coatings, Surf. Coat. Technol. 381 (2020) 125107, https://doi.org/10.1016/j.surfcoat.2019.125107.
[8] H. Zhao, C.G. Levi, H.N.G. Wadley, Vapor deposited samarium zirconate thermal barrier coatings, Surf. Coat. Technol. 203 (2009) 3157–3167, https://doi.org/10.1016/j.surfcoat.2009.03.048.
[9] B. Saruhan, P. Francois, K. Fritscher, U. Schulz, EB-PVD processing of pyrochlore-structured La2Zr2O7-based TBCs, Surf. Coat. Technol. 182 (2004) 175–183, https://doi.org/10.1016/j.surfcoat.2003.08.068.
[10] U. Schulz, W. Braue, Degradation of La2Zr2O7 and other novel EB-PVD thermal barrier coatings by CMAS (CaO-MgO-Al2O3-SiO2) and volcanic ash deposits, Surf. Coat. Technol. 235 (2013) 165–173, https://doi.org/10.1016/j.surfcoat.2013.07.029.
[11] U. Schulz, B. Saruhan, K. Fritscher, C. Leyens, Review on advanced EB-PVD ceramic topcoats for TBC applications, Int. J. Appl. Ceram. Technol. 1 (2004) 302–315, https://doi.org/10.1111/j.1744-7402.2004.tb00182.x.
[12] Z. Xu, L. He, X. Chen, Y. Zhao, X. Cao, Thermal barrier coatings of rare earth materials deposited by electron beam-physical vapor deposition, J. Alloys Compd. 508 (2010) 94–98, https://doi.org/10.1016/j.jallcom.2010.04.160.
[13] M.P. Schmitt, J.L. Stokes, B.L. Gorin, A.K. Rai, D. Zhu, T.J. Eden, D.E. Wolfe, Effect of Gd content on mechanical properties and erosion durability of sub-stoichiometric Gd2Zr2O7, Surf. Coat. Technol. 313 (2017) 177–183, https://doi.org/10.1016/j.surfcoat.2016.12.045.
[14] J.R. Nicholls, Y. Jaslier, D.S. Rickerby, Erosion of EB-PVD thermal barrier coatings, Mater. High Temp. 15 (1998) 15–22, https://doi.org/10.1080/09603409.1998.11689572.
[15] ASTM, ASTM G76–18 Standard Test Method for Conducting Erosion Tests by Solid Particle Impingement Using Gas Jets 1, 2018, https://doi.org/10.1520/G0076-18.
[16] ASTM, ASTM G40–22 Standard Terminology Relating to Wear and Erosion, 2022, https://doi.org/10.1520/G0040-22.
[17] J. Chevallier, L. Isern, K. Almandoz Forcen, C. Chalk, J.R. Nicholls, Modelling evaporation in electron-beam physical vapour deposition of thermal barrier coatings, Emerg. Mater. (2021), https://doi.org/10.1007/s42247-021-00284-5.
[18] K. Almandoz Forcen, L. Isern, A. Johnstone, G. Brewster, J.R. Nicholls, C. Chalk, Automated columnar microstructure analysis using CoCo (column counter): Insights from EB-PVD TBCs, Surf. Coat. Technol. (2025) 132998, https://doi.org/10.1016/j.surfcoat.2025.132998.
[19] U. Schulz, K. Fritscher, C. Leyens, M. Peters, W.A. Kaysser, Thermocyclic behavior of differently stabilized and structured EB-PVD TBCs 49 (1997) https://www.tms.org/pubs/journals/JOM/9710/Schulz/Schulz-9710.html.
[20] C. Mikulla, L. Steinberg, P. Niemeyer, U. Schulz, R. Naraparaju, Microstructure refinement of EB-PVD gadolinium Zirconate thermal barrier coatings to improve their CMAS resistance, Coatings 13 (2023), https://doi.org/10.3390/coatings13050905.
[21] A.U. Munawar, U. Schulz, G. Cerri, H. Lau, Microstructure and cyclic lifetime of Gd and Dy-containing EB-PVD TBCs deposited as single and double-layer on various bond coats, Surf. Coat. Technol. 245 (2014) 92–101, https://doi.org/10.1016/j.surfcoat.2014.02.047.
[22] J.L. Payne, M.G. Tucker, I.R. Evans, From fluorite to pyrochlore: characterisation of local and average structure of neodymium zirconate, Nd2Zr2O7, J. Solid State Chem. 205 (2013) 29–34, https://doi.org/10.1016/j.jssc.2013.07.001.
[23] G.R. Lumpkin, R.D. Aughterson, Perspectives on Pyrochlores, defect fluorites, and related compounds: building blocks for chemical diversity and functionality, Front. Chem. 9 (2021), https://doi.org/10.3389/fchem.2021.778140.
[24] U. Brykała, R. Diduszko, K. Jach, J. Jagielski, Hot pressing of gadolinium zirconate pyrochlore, Ceram. Int. 41 (2015) 2015–2021, https://doi.org/10.1016/j.ceramint.2014.09.114.
[25] T. Kember, Compositional Variations in Vapor Deposited Samarium Zirconate Coatings, MSc Thesis, University of Virginia, 2011.
[26] U. Schulz, B. Saruhan, K. Fritscher, C. Leyens, Review on advanced EB-PVD ceramic topcoats for TBC applications, Int. J. Appl. Ceram. Technol. 1 (2004) 302–315, https://doi.org/10.1111/j.1744-7402.2004.tb00182.x.
[27] U. Schulz, M. Schmücker, Microstructure of ZrO2 thermal barrier coatings applied by EB-PVD, Mater. Sci. Eng. A (2000), https://doi.org/10.1016/S0921-5093(99)00576-6.
[28] J.A. Thornton, High rate thick film growth, Annu. Rev. Mater. Sci. 7 (1977) 239–260, https://doi.org/10.1146/annurev.ms.07.080177.001323.
[29] C. Gatzen, D.E. Mack, O. Guillon, R. Vaßen, YAlO3-a novel environmental barrier coating for Al2O3/Al2O3-ceramic matrix composites, Coatings 9 (2019), https://doi.org/10.3390/coatings9100609.
[30] V.R. Khrustov, A.S. Kaygorodov, S.V. Zayats, The thermal expansion of lanthanum Zirconate ceramics, Inorg. Mater. Appl. Res. 16 (2025) 1333–1337, https://doi.org/10.1134/S2075113325701400.
[31] J.A.J. Ball, J.F. Martins, G. Brewster, Y. Chen, P. Xiao, An investigation into RESZ (RE = Yb, Er, Gd, Sm) materials for CMAS resistance in thermal barrier coatings, J. Eur. Ceram. Soc. 44 (2024) 3734–3746, https://doi.org/10.1016/j.jeurceramsoc.2024.01.041.
[32] S. Mahade, N. Curry, S. Björklund, N. Markocsan, P. Nylén, R. Vaßen, Erosion performance of gadolinium Zirconate-based thermal barrier coatings processed by suspension plasma spray, J. Therm. Spray Technol. 26 (2017) 108–115, https://doi.org/10.1007/s11666-016-0479-4.
[33] J.R. Nicholls, M.J. Deakin, D.S. Rickerby, A comparison between the erosion behaviour of thermal spray and electron beam physical vapour deposition thermal

barrier coatings, Wear 233–235 (1999) 352–361, https://doi.org/10.1016/S0043-1648(99)00214-8.
[34] R.G. Wellman, M.J. Deakin, J.R. Nicholls, The effect of TBC morphology on the erosion rate of EB PVD TBCs, Wear 258 (2005) 349–356, https://doi.org/10.1016/j.wear.2004.04.011.
[35] R.G. Wellman, J.R. Nicholls, A review of the erosion of thermal barrier coatings, J. Phys. D. Appl. Phys. 40 (2007), https://doi.org/10.1088/0022-3727/40/16/R01.



https://dspace.org/

Improving the manufacturability and assessing the performance of rare earth zirconates for thermal barrier coatings

Isern, Luis; Almandoz Forcen, Koldo; Chalk, Christine; Brewster, Gyaneshwara; Johnstone, Alan ...

2026-02-01
Elsevier
https://doi.org/10.1016/j.surfcoat.2025.133137
Isern L, Almandoz Forcen K, Chalk C, et al., (2026) Improving the manufacturability and assessing the performance of rare earth zirconates for thermal barrier coatings. Surface and Coatings Technology, Volume 521, February 2026, Article number 133137

Downloaded from a DSpace repository. https://dspace.org/